Journal of
Composites Science

MDPI

Article

Photocatalytic Performance of the Synergetic Coupling of NiO-MgO Nanostructures on a g-C_3N_4 Composite Towards Methylene Blue Under Visible-Light Irradiation

Shaojun Hao [1], Siew Wen Ching [1], Timm Joyce Tiong [1], Yeow Hong Yap [2] and Chao-Ming Huang [3,*]

[1] Department of Chemical and Environmental Engineering, University of Nottingham Malaysia, Jalan Broga, Semenyih 43500, Selangor, Malaysia
[2] Department of Chemical Engineering, Lee Kong Chian Faculty of Science and Engineering, Universiti Tunku Abdul Rahman, Jalan Sungai Long, Bandar Sungai Long, Kajang 43000, Selangor, Malaysia
[3] Department of Advanced Applied Materials Engineering, Kun Shan University, No. 195, Kunda Rd., Yongkang Dist., Tainan 71007, Taiwan
* Correspondence: charming@mail.ksu.edu.tw

Abstract

In this study, a ternary Ni/Mg/g-C_3N_4 composite was synthesized via a controlled precipitation–calcination route and evaluated for its visible-light-assisted degradation of methylene blue (MB). The structural, morphological, and optical characteristics of the composites were systematically investigated using XRD, FT-IR, FESEM, BET, and UV–Vis analyses. The results confirmed the successful construction of Ni/Mg/g-C_3N_4 heterojunctions with strong interfacial coupling and enhanced surface porosity. Among all samples, the Ni/Mg/CN20 composite exhibited the highest activity, achieving 66% MB degradation within 180 min under visible light. This superior performance was attributed to synergistic effects arising from efficient interfacial charge transfer, broadened light absorption, and abundant active sites. The composite also displayed excellent thermal stability. This work demonstrates that the rational control of g-C_3N_4 loading plays a decisive role in tuning the physicochemical and catalytic properties of Ni/Mg/g-C_3N_4 composites. The findings provide new insights into the design of cost-effective, thermally stable, and high-performance photocatalysts for visible-light-driven wastewater treatment.

Keywords: nickel catalyst; magnesium catalyst; g-C_3N_4; methylene blue; photocatalysis

Academic Editor: Weidong He

Received: 26 November 2025
Revised: 7 January 2026
Accepted: 9 January 2026
Published: 13 January 2026

1. Introduction

With the rapid advancement of global industrialization and urbanization, synthetic dyes are increasingly used in textiles, printing and dyeing, papermaking, plastics, cosmetics, food, and pharmaceuticals. According to statistics, the textile industry is the primary consumer of dyes worldwide, accounting for more than half of total usage [1,2]. During dyeing and printing processes, large amounts of dye-containing wastewater are discharged without adequate treatment, resulting in severe water pollution. Synthetic dyes typically have complex aromatic structures and excellent chemical stability [3–6]. While these properties endow them with excellent coloring properties, they also render them extremely resistant to degradation in the natural environment [7,8]. Consequently, they accumulate in water bodies over long periods of time, causing reduced light penetration, inhibition of photosynthetic activity, and disruption of aquatic ecosystems. Methylene blue (MB) is a common cationic dye widely used in textile printing [9,10] and dyeing [7], medical

diagnostics [11,12], and biochemical analysis due to its vivid color [13], excellent stability, and significant color development ability even at extremely low concentrations. However, MB's high chemical stability and poor biodegradability make it a typical persistent organic pollutant, allowing it to remain in water and soil by adsorbing onto suspended particles or sediments [14]. Moreover, research has shown that MB and its degradation intermediates are toxic and mutagenic to aquatic organisms and even humans [15]. Consequently, developing efficient, economical, and environmentally friendly technology for MB removal has become a critical and pressing issue in environmental remediation.

Photocatalysis has emerged as one of the most promising technologies for degrading organic pollutants under mild conditions due to its high efficiency, low energy consumption, and environmental friendliness [16,17]. In recent years, composite materials that integrate multiple functional components have been widely developed to enhance the photocatalytic degradation of organic pollutants, as their synergistic interfaces can facilitate charge transfer, increase active surface sites, and improve structural stability under operational conditions [18]. For instance, g-C_3N_4/BiOI heterojunctions showed efficient dye removal due to improved charge separation [19], while Ga_2S_3/g-C_3N_4 composites exhibited enhanced activity by suppressing recombination [20]. Similarly, MOF-based composites provided abundant active sites and superior photodegradation of wastewater dyes [21].

Nickel-based materials, in particular, have attracted considerable attention due to their excellent electronic structure tunability and diverse chemical states [22,23]. In photocatalytic systems, nickel-based compounds are typically considered co-catalysts. Despite their low intrinsic photocatalytic activity, they can significantly enhance the photocatalytic performance of primary catalysts (such as TiO_2 or g-C_3N_4) by promoting the efficient separation of photogenerated electrons and holes [24–27]. Interestingly, recent studies have demonstrated that some nickel-based compounds can not only act as co-catalysts but also directly drive photocatalytic reactions [28], either independently or as active components in heterojunction structures [29]. Nickel oxide (NiO), a typical p-type transition metal oxide, is widely used in energy conversion and pollution control due to its excellent chemical stability, abundant oxygen vacancy structure, and high electrochemical activity. Its narrow band gap (approximately 3.4 eV) endows the material with strong visible-light responsiveness, making NiO a promising standalone photocatalyst or electron acceptor component in composite systems. NiO can effectively promote charge separation through heterojunction formation [26,30,31], and its nanostructures (such as nanosheets [32], nanoflowers [33], and hollow spheres [34]) provide abundant active sites for the reaction. Moreover, oxygen vacancies in NiO can serve as free radical generation centers, promoting the production of reactive species such as •OH and $\bullet O_2^-$, and further enhancing photocatalytic activity [35]. Notably, its excellent stability and recyclability [36,37] render NiO a promising and sustainable photocatalyst for practical wastewater treatment applications.

Magnesium-based oxides, particularly MgO, have also drawn widespread attention in recent years due to their low cost, environmental friendliness, and excellent physicochemical properties. MgO possesses a high specific surface area, tunable crystal structure, and abundant surface oxygen vacancies, which endow it with excellent adsorption properties and active site density [38–40]. Compared with other metal oxide catalysts (such as TiO_2 [37,41], ZnO [42], and Fe_2O_3 [43]), MgO has a larger band gap (approximately 5.0–7.8 eV) and exhibits strong oxidizing ability under UV light or in composite systems. The strong surface alkalinity of MgO helps in generating hydroxyl radicals (•OH) and accelerating the degradation of pollutant molecules. Furthermore, its excellent thermal stability and chemical inertness prevent deactivation during prolonged reactions [44], and its

non-toxic nature prevents secondary pollution [45]. Therefore, MgO serves as a promising co-catalyst and structural stabilizer in composite photocatalytic systems.

Despite the advantages of nickel- and magnesium-based oxides, their practical application remains constrained by intrinsic limitations. Ni-based compounds generally suffer from narrow band gaps, limited light absorption ranges, and high recombination rates of photogenerated carriers, resulting in low efficiency in the visible-light region. Furthermore, some Ni-based materials are prone to valence-state transitions (Ni^{2+}/Ni^{3+}) under illumination or electrochemical conditions [46], resulting in decreased catalytic activity and insufficient stability after long-term reactions. On the other hand, MgO's wide band gap (approximately 4.2–9 eV) and near-invisible light responsiveness limit its application in solar-driven photocatalysis. Furthermore, MgO has low electron mobility, and surface defects are easily occupied or passivated during the reaction, resulting in the rapid recombination of photogenerated electron–hole pairs and reduced overall catalytic efficiency. Recent breakthroughs in advanced oxidation processes (AOPs) have highlighted the significance of atomic-level structural engineering. For instance, Yang et al. [47] demonstrated that superstructures with arranged perovskite and oxide layers can significantly enhance non-free radical pathways, which are less susceptible to interference from background electrolytes in wastewater. This underscores the critical importance of designing well-defined heterostructures and interfacial environments to optimize catalytic performance and selectivity. To address these challenges, constructing a heterojunction with visible-light-responsive semiconductors has proven effective [48]. Graphitic carbon nitride (g-C_3N_4) with a moderate band gap (approximately 2.7 eV) and excellent thermal and chemical stability [49] has emerged as an ideal candidate. g-C_3N_4 possesses a two-dimensional layered structure composed of triazine or triazineamide units [50–52], which provides nitrogen sites for adsorption and electron transfer. However, pure g-C_3N_4 still exhibits limited conductivity [53] and high recombination rates of photogenerated carriers.

To overcome these shortcomings, this study proposes the use of transition metal oxides to construct heterojunctions to achieve the synergistic effect of energy band matching and interface charge separation. The composite of g-C_3N_4 with metal oxides such as NiO [54,55] and MgO [56] can not only form a stable p-n junction structure at the interface but also utilize the energy band gap between the two to promote the directional migration of photogenerated electrons and holes, significantly reduce the probability of recombination, and improve photocatalytic efficiency. The Ni-based component acts as an electron capture center to enhance electron conduction, while the alkaline surface and abundant oxygen vacancies of MgO are conducive to the adsorption and activation of pollutant molecules. Through this ROS synergistic mechanism, this composite strategy not only effectively makes up for the shortcomings of the performance of a single material but also provides a new design method for constructing an efficient, stable, and environmentally friendly photocatalytic degradation system.

2. Materials and Methods

2.1. Catalyst Synthesis

All chemical reagents used in this study were of analytical grade and used without further purification. Magnesium sulfate heptahydrate ($MgSO_4 \cdot 7H_2O$, 99%), nickel sulfate hexahydrate ($NiSO_4 \cdot 6H_2O$, 99 wt%), sodium carbonate (Na_2CO_3, 10 wt%), and urea were purchased from R&M Chemicals (Subang Jaya, Malaysia). Methylene blue (MB) was supplied by Sigma Aldrich (Petaling Jaya, Malaysia). Deionized water (Milli-Q Advantage A10 Ultrapure Water Purification System, resistivity of 18.2 MΩ·cm, Millipore, Burlington, MA, USA) was used throughout the experiments.

A mixed solution of nickel sulfate hexahydrate ($NiSO_4 \cdot 6H_2O$) and magnesium sulfate heptahydrate ($MgSO_4 \cdot 7H_2O$) with a molar ratio of 3:1 was prepared and heated to 50 °C under continuous stirring. Sodium carbonate (Na_2CO_3, 10 wt%) was then added dropwise, and the reaction was allowed to proceed for 30 min. The pH of the suspension was subsequently adjusted and maintained during stirring for an additional 30 min to ensure complete precipitation.

The resulting precipitate was collected by filtration, repeatedly washed with deionized water to remove residual ions, and dried in an oven at 100 °C for 5 h. The dried powder was finally calcined in a muffle furnace at 400 °C for 4 h to obtain the catalyst precursor. Separately, urea powder was distributed evenly within a 50 mL alumina crucible, covered, and placed within the muffle furnace. The heating program was set to raise the temperature from room temperature to 550 °C at a rate of 5 °C/min and then maintained at this temperature for 2 h. Once the muffle furnace had cooled to room temperature, the sample was removed from the crucible. Graphite-like layered g-C_3N_4 was then formed, with the system's color gradually changing from white to pale yellow, ultimately yielding a block-like solid. Carbon nitride and the nickel–magnesium complex obtained after the reaction were rinsed in deionized water. Following ultrasonication, the resulting suspension was transferred to an oven and reacted at 100 °C for 12 h. The final dried product, after grinding, yielded the target compound. For the composite products, the mixed metal salt precursors and respective 10, 20, and 30 wt% of graphitic carbon nitride were dissolved in deionized water. The mixture was ultrasonically stirred and subsequently treated in a similar manner to those used in the absence of g-C_3N_4 and then dried at 120 °C for 8 h to obtain the target composites of Ni/Mg/CN10, Ni/Mg/CN20, and Ni/Mg/CN30.

2.2. Experimental Procedure

An appropriate quantity of MB solid was weighed to prepare a stock solution (e.g., 100 mg/L), which was diluted to obtain a working solution of the target concentration (e.g., 10 mg/L). Each reaction flask in this experiment holds 150 mL of liquid. Then, 0.075 g (75 mg) of the catalyst was added to each 150 mL bottle of MB solution at a dosage of 0.5 g/L and mixed thoroughly using magnetic stirring.

The suspension was stirred for 30 min under light-protected conditions to achieve adsorption–desorption equilibrium between the catalyst and MB. After sampling and filtration (or centrifugation), the initial absorbance (or concentration C_0) at 664 nm was determined using UV-Vis spectroscopy. The reaction system was exposed to visible light under a light source maintained at a fixed distance (e.g., 15 cm) above the liquid surface, with continuous stirring throughout. At fixed intervals (e.g., 15 min), a sample was collected via filtration, and the absorbance at 664 nm (C_t) was determined. For comparisons, blank experiments were also performed under identical conditions: in the dark (adsorption control). These control tests confirmed that MB degradation was negligible without both light and the catalyst, demonstrating that the observed activity originated from the photocatalytic process.

2.3. Methylene Blue Degradation

The photocatalytic degradation efficiency of MB was quantitatively evaluated using UV-visible spectroscopy (UV-vis, Perkin Elmer Lambda 35, Perkin Elmer, Waltham, MA, USA) based on the changes in absorbance at a single-point wavelength of 664 nm measured at defined time intervals. The degradation rate was calculated according to the following equation:

$$Degradation\ rate(\%) = (1 - C_t/C_0) \times 100\%$$

where C_0 represents the initial concentration of the MB solution after adsorption–desorption equilibrium in the dark, and C_t denotes the concentration at time t during photocatalytic illumination. For normalization, the degradation efficiency was also expressed as C/C_0, providing a relative comparison across different catalysts.

To further analyze the photocatalytic kinetics, the experimental data were fitted to a pseudo-first-order kinetic model, which is widely employed in heterogeneous photocatalysis due to its reliability in dilute pollutant systems. The model is expressed as follows:

$$\ln(C_0/C_t) = kt$$

where k is the apparent first-order reaction rate constant (min^{-1}). By plotting $\ln(C_0/C_t)$ against reaction time, the slope of the linear fit was used to determine k. Higher values of k indicate faster degradation rates and superior catalytic performance.

In addition to the pseudo-first-order model, alternative kinetic models such as the Langmuir–Hinshelwood (L–H) model were considered to account for surface adsorption effects, especially in the initial stages of the reaction. The L–H model assumes that the reaction rate is proportional to the fraction of pollutant molecules adsorbed on the catalyst surface and can be represented as follows:

$$r = \frac{kKC}{1 \pm KC}$$

where r is the reaction rate, k is the intrinsic reaction constant, K is the adsorption equilibrium constant, and C is the pollutant concentration. This model allows for a more accurate description of the catalytic process when adsorption plays a dominant role.

2.4. Catalyst Characterisation

2.4.1. X-Ray Powder Diffraction (XRD)

The structure and microstructure of the samples were evaluated using a Bruker D6 Phaser X-ray diffractometer (Billerica, MA, USA) (Cu-Kλ radiation; 1.5406 Å). The measurement and evaluation software used was Diffrac.Eva (Karlsruhe, Germany), respectively. The measurement step size was 0.03°, and the time/step was 0.5 s. The samples were analyzed as pellets pressed on a laboratory press. XRD spectra were acquired over the 2θ range of 5° to 70°.

2.4.2. Field Emission Scanning Electron Microscopy (FE-SEM)

The surface morphology of the samples was characterized using a scanning electron microscope (SEM, FEI Quanta 400F, Hillsboro, OR, USA). The dried powder sample was evenly dispersed on a conductive adhesive and then sputtered with a gold film approximately 5 nm thick to enhance conductivity. The test was conducted under high-vacuum conditions with an accelerating voltage set between 5 and 15 kV to obtain microstructural images of the samples at various magnifications. SEM images reveal information such as particle morphology, size distribution, and surface roughness, enabling analyses of the microstructural characteristics and the morphological differences in the samples.

2.4.3. Energy Dispersive X-Ray (EDX) Analysis

To further confirm the elemental composition and distribution of the samples, elemental analysis was performed using an energy-dispersive X-ray spectrometer (EDS, supplied with a SEM, Model INCA 400, Oxford Instruments, Abingdon, UK). The analysis was conducted under high-vacuum conditions, using an accelerating voltage of 15 kV and an acquisition time of approximately 60 s. EDS spectra can be used to determine the identity and relative content of the main elements in the samples. Elemental mapping images can

also be used to analyze the spatial uniformity of the elements on the material surface. The results show that the elements in the prepared samples are uniformly distributed, with no apparent agglomeration or segregation, further verifying the successful construction of the composite material.

2.4.4. Brunauer–Emmett–Teller (BET) Analysis

The specific surface area and pore structure characteristics of the samples were determined via nitrogen adsorption–desorption experiments using the Micromeritics ASAP 2020 surface area analyzer (Norcross, GA, USA). Prior to testing, the samples were vacuum-degassed at 150 °C for 6 h to remove adsorbed water and impurities on the surface and within the pores. The tests were conducted at liquid nitrogen temperature (77 K). The specific surface area was calculated using the Brunauer–Emmett–Teller (BET) equation, and the pore size distribution curve was obtained using the Barrett–Joyner–Halenda (BJH) method. These results can be used to analyze the specific surface area, pore structure type, and distribution characteristics of the materials, providing important structural evidence for their photocatalytic performance.

2.4.5. Fourier Transform Infrared Spectroscopy (FT-IR)

The chemical bonding characteristics and functional group composition of the samples were characterized using Fourier transform infrared spectroscopy (FTIR, Perkin Elmer Frontier FTIR, Shelton, CT, USA). The measurement range was 4000–400 cm^{-1}, and the samples were prepared using the KBr pellet method. Analysis of the characteristic absorption peaks in the spectrum reveals the primary chemical bonding types on the material surface and the interactions between the different components. This further verifies the successful bonding of the components in the composite system and their chemical structure.

2.4.6. Thermogravimetric Analysis (TGA)

Thermogravimetric analysis (TGA) was performed using a Mettler Toledo TGA/DSC thermogravimetric analyzer (Greifensee, Switzerland). A 1–2 mg sample was placed in a platinum pan. Under a nitrogen flow rate of 25 mL/min, the sample was heated from 200 to 1000 °C at a heating rate of 25 °C/min, and weight loss was recorded. Weight curves were plotted using Origin software (Version 2024, Boston, MA, USA).

3. Results

3.1. XRD Analysis

Figure 1 presents the X-ray diffraction (XRD) pattern of the Ni/Mg/g-C_3N_4 composite. Characteristic diffraction peaks for each component within the composite material are clearly discernible, providing a direct reflection of the crystalline structure and dispersion state of each phase. The XRD pattern of the composite catalyst reveals characteristic NiO diffraction peaks at approximately 2θ = 37.2° and 43.3°, corresponding to the (111) and (200) crystal planes of NiO, respectively [57]. Characteristic diffraction peaks for MgO appear at approximately 2θ = 42.9° and 62.3°, corresponding to the (200) and (220) crystal planes of MgO [58]. To further investigate the effect of Ni doping on the lattice structure, an enlarged view of the 2θ = 19°peak is provided in Figure 1b. A subtle shift towards higher 2θ angles is observed in the Ni-doped samples compared to pure MgO (ICDD card #01-077-2364) and NiO (ICDD card #01-073-1523). Concurrently, characteristic diffraction peaks of g-C_3N_4 were observed at approximately 12.9° and 27.6° 2θ, corresponding to its (100) and (002) crystal planes, respectively [59]. This indicates that the composite catalyst still retains some of the (002) crystalline structure.

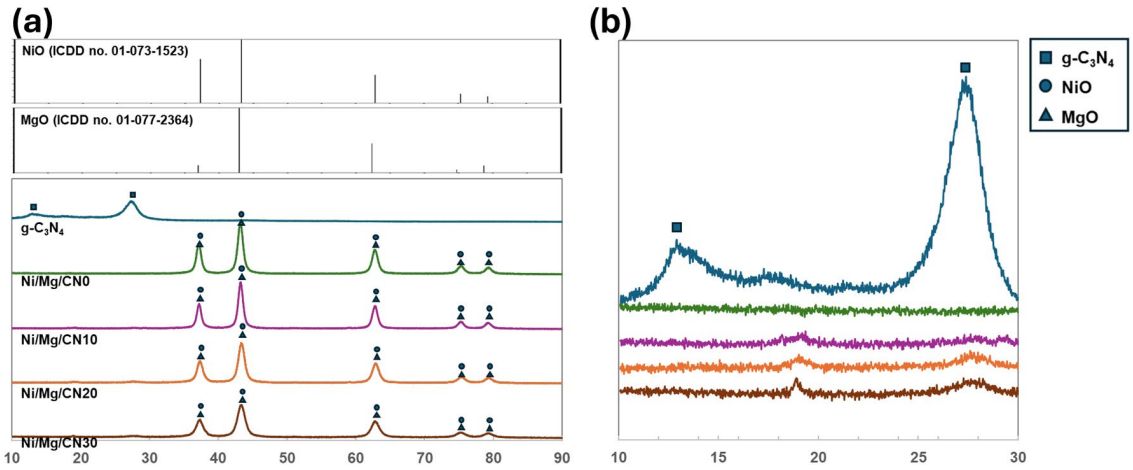

Figure 1. (**a**) XRD diffractogram of the samples and (**b**) magnified XRD diffractogram of characteristic peaks at 2θ from 10 to 30 degrees.

XRD patterns show that the intensities of the characteristic diffraction peaks of NiO and MgO vary with the Ni and Mg content or preparation conditions. Ni/Mg precursors doped with different weight percentages of carbon nitride (10 wt%, 20 wt%, and 30 wt%), hereinafter referred to as Ni/Mg/CN10, Ni/Mg/CN20, and Ni/Mg/CN30, exhibit sharp and intense NiO and MgO diffraction peaks when the Ni and Mg content reaches an optimal balance at 10 wt%, indicating good crystallinity. While there was no observable shift in NiO or MgO peaks upon the addition of g-C_3N_4, with reference to Figure 1b, a small apparent peak at ~19.5° becomes gradually more visible as CN content increases, which may be attributed to the incomplete crystallization of Ni/Mg oxides and the presence of residual hydroxide phases such as $Ni(OH)_2$ or $Mg(OH)_2$ [60]. In addition, a slight increase in the intensity of the g-C_3N_4 (002) reflection at ~27.6° is observed with higher CN loading, confirming the progressive incorporation of CN into the composite framework [61]. However, the results revealed that excessively high g-C_3N_4 content resulted in broadened diffraction peaks and diminished peak intensities. This suggests that the incorporation of g-C_3N_4 into the Ni-Mg matrix does not scale linearly with its loading. The phenomenon is likely attributed to saturation of active binding sites, agglomeration of g-C_3N_4 particles, and poor dispersion at elevated concentrations. Once the surface capacity of the Ni-Mg substrate is exceeded, surplus g-C_3N_4 may remain unbound or form aggregates, which are less likely to integrate effectively into the composite structure. This behavior has been documented in prior studies, where excessive g-C_3N_4 loading was shown to hinder uniform distribution and reduce functional performance due to particle clustering and limited interfacial interaction [62–64]. Furthermore, the characteristic peaks of g-C_3N_4 persist within the composite. Although only the (002) diffraction of g-C_3N_4 showed prominent peaks in the composite XRD, FT-IR results later confirmed the presence of g-C_3N_4 and its bonding environment, indicating that g-C_3N_4 exists as poorly crystalline or exfoliated layers dispersed on NiO/MgO. These layers coexist with those of NiO and MgO, therefore confirming the successful incorporation of all three phases within the composite without significant chemical reactions forming new phases. This composite structure facilitates synergistic effects among the components during photocatalytic and other reactions.

3.2. FESEM Analysis

Figure 2 presents the field-emission scanning electron micrograph (FESEM) of the composites, where Figure 2a–c represent the morphologies of NiO, MgO, and g-C_3N_4, respectively, followed by Ni/Mg with different g-C_3N_4 doping amounts of 10 wt%, 20 wt%, and 30 wt% in Figure 2d–f. Based on Figure 2c, it can be observed that carbon nitride (g-

C_3N_4) exhibited a characteristic porous layered or foamy surface structure with numerous pores and folds. This aligned with the thermal polymerization synthesis process, wherein the layered structure facilitates light absorption and charge separation [65–67]. Functioning as a carrier or primary catalyst, g-C_3N_4 provided a high specific surface area and visible-light responsiveness.

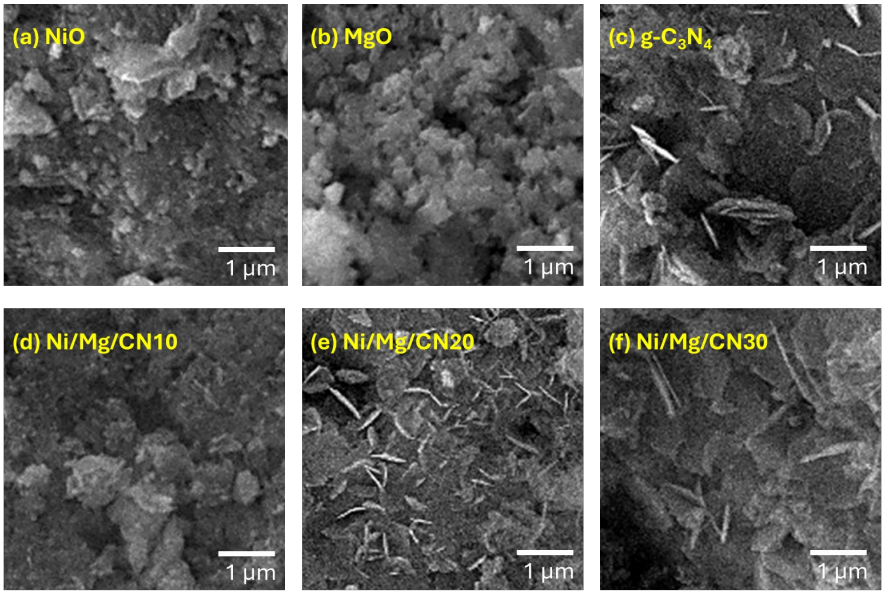

Figure 2. (**a**) FESEM image of NiO, (**b**) FESEM image of MgO, (**c**) FESEM image of g-C_3N_4, (**d**) FESEM image of Ni/Mg/CN10, (**e**) FESEM image of Ni/Mg/CN20, and (**f**) FESEM image of Ni/Mg/CN30.

Figure 2d–f depicts a nickel–magnesium composite with varying carbon nitride contents. The overall trend showed that as carbon nitride contents increased, the composite morphology transitioned from particle agglomeration (Figure 2d) towards a more uniform supported structure (Figure 2e,f). Figure 2d exhibited low amounts of needle-like structures, suggesting the low doping level of carbon nitride. On the other hand, Figure 2e shows that the sample started to exhibit a more significant amount of needle-like structures, suggesting a higher percentage of carbon nitride in the sample. However, it can also be observed that these structures were still centralized around a particular area, suggesting that agglomeration is still occurring within the sample. Extending from this, Figure 2f shows the higher dispersion of carbon nitride, whereby the needle-like structure representing the formation of carbon nitride seemed to be more dispersed across the Ni/Mg composite. Despite earlier XRD results showing the poor presence of crystallite g-C_3N_4 in samples containing 20 and 30 wt% of g-C_3N_4, the FESEM images clearly showed otherwise, signifying the probable occurrence of amorphous g-C_3N_4 as loading increased.

3.3. EDX Analysis

The mapping in Figure 3 confirms the elements present in the SEM images, whereby the needle-like structures highly correlate with carbon and nitrogen, while the spherical or round agglomerates represent the composites of Ni, Mg, and O. This distinctive comparison highlights the successful integration of g-C_3N_4 within the Ni–Mg matrix, where the elongated carbon–nitrogen features suggest well-dispersed g-C_3N_4 domains, and the rounded clusters correspond to the oxide phases of Ni and Mg. The coexistence of these morphologies indicates a heterogeneous distribution, yet with clear elemental segregation that supports the proposed composite structure. Similar needle-like morphologies of g-C_3N_4 have been reported in the literature, attributed to supramolecular self-assembly and thermal polycondensation processes, which promote anisotropic growth and enhance sur-

face activity [62,68,69]. Such mappings not only validate the XRD findings but also provide direct evidence of the synergistic interaction between the g-C_3N_4 framework and Ni–Mg oxide particles. The observed microstructural contrast further implies that g-C_3N_4 acts as a scaffold, promoting the dispersion of metallic oxides while simultaneously contributing to enhanced surface activity and the stability of the composite.

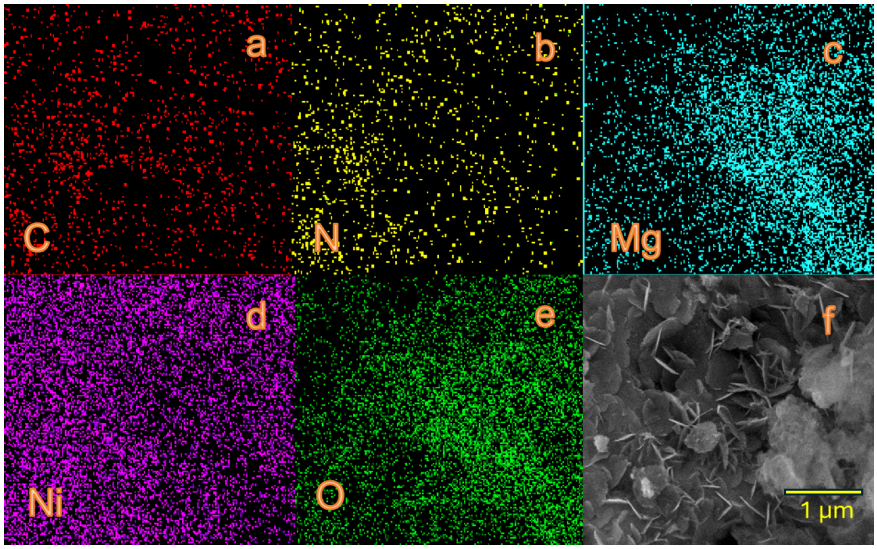

Figure 3. Elemental mapping of (**a**) carbon, (**b**) nitrogen, (**c**) magnesium, (**d**) nickel, and (**e**) oxygen for the FESEM image of Ni/Mg/CN20, (**f**) FESEM image of Ni/Mg/CN20.

3.4. BET Analysis

The BET surface area and pore structure analysis summarized in Table 1 highlight the influence of g-C_3N_4 loading on the Ni/Mg composite. The pristine Ni/Mg composite shows a moderate surface area (67.9 m^2/g) with a relatively large average pore width (62.193 Å), characteristic of mesoporous materials. When 10 wt% g-C_3N_4 is introduced (Ni/Mg/CN10), the surface area decreases to 51.8 m^2/g, while the pore width expands significantly (85.551 Å). This suggests that at low loading, g-C_3N_4 particles partially block pores and create irregular voids, reducing the accessible surface area but enlarging average pore sizes. Similar pore-blocking effects at low g-C_3N_4 incorporation have been reported by Durmus, et al. [70], who observed narrowed pore diameters and altered pore volumes in Ce-MOF/g-C_3N_4 composites.

Table 1. Structural properties and physical absorption of the catalyst.

Catalyst	BET Surface Area (m^2/g)	BJH Desorption Average Pore Width (Å)
Ni/Mg	67.9238	62.193
Ni/Mg/CN10	51.7538	85.551
Ni/Mg/CN20	91.6530	61.186
Ni/Mg/CN30	112.0394	51.527

At 20 wt% loading (Ni/Mg/CN20), the surface area increases sharply to 91.7 m^2/g, with a balanced pore width (61.186 Å). This indicates the more effective dispersion of g-C_3N_4 within the Ni/Mg matrix, generating additional mesopores and preventing dense particle packing. The Ni/Mg/CN20 sample thus achieves the optimal compromise between surface area and pore accessibility, which explains its superior catalytic performance. Comparable BET values have been reported for porous g-C_3N_4 prepared by thermal

polymerization, where Yang, et al. [71] achieved surface areas up to 120 m^2/g with pore widths in the range of 70–100 nm. The similarity in pore size distribution confirms that Ni/Mg/CN20 falls within the optimal mesoporous regime.

At higher loading (Ni/Mg/CN30), the surface area further increases (112.0 m^2/g), but the average pore width decreases (51.527 Å), implying that excess g-C_3N_4 begins to narrow the pores, potentially limiting diffusion despite the larger surface area. This trend is consistent with reports by Dong, Yang, ullah, irshad and Xue [68], who showed that morphological changes in g-C_3N_4 alter pore distribution and accessibility, emphasizing that excessive loading can compromise pore uniformity.

Overall, this nonlinear trend demonstrates that pore size distribution and accessibility are as critical as surface area in determining catalytic efficiency. The Ni/Mg/CN20 sample provides sufficient surface area with well-distributed mesopores, facilitating mass transfer and exposure of active sites, in agreement with the mesoporous ranges reported in the literature.

The pore size distribution profiles in Figure 4, together with the BET data in Table 1, highlight the effect of g-C_3N_4 loading on the Ni/Mg composites. In general, all samples exhibited dominant mesopores in the 50–100 Å range, consistent with values reported for g-C_3N_4-based composites [71]. The Ni/Mg/CN20 sample exhibited a slightly shifted distribution, with its peak centered around 80–150 Å. This shift suggests that at 20 wt% loading, g-C_3N_4 is more effectively dispersed within the Ni/Mg matrix, generating mesopores that are both accessible and well-connected. Reports in the literature indicate that mesopores in the 80–150 Å range are particularly favorable for photocatalytic and adsorption processes, as they provide sufficient space for reactant diffusion while maintaining close proximity to active sites [63,70]. Therefore, the data probably suggests that Ni/Mg/CN20 achieves a pore size distribution that is more conducive to catalytic activity compared to the other samples.

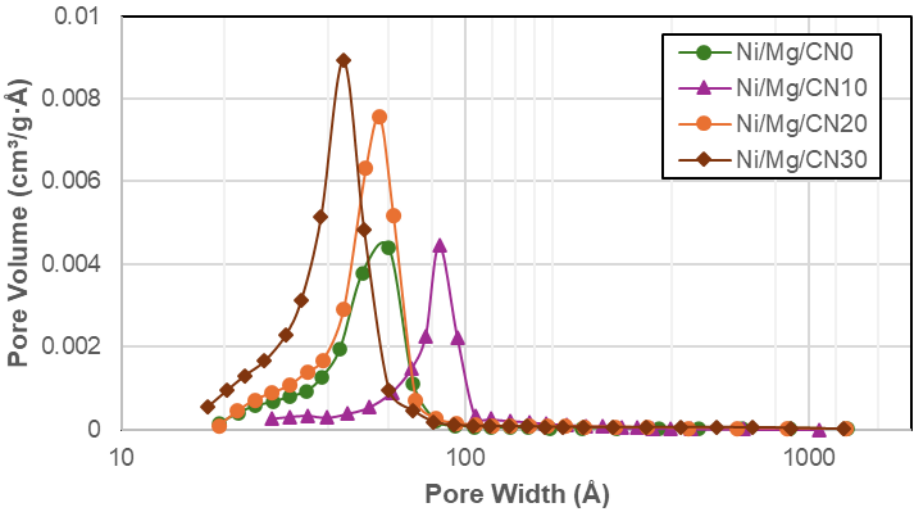

Figure 4. Pore size distribution of the composite.

In contrast, Ni/Mg/CN30, despite exhibiting the largest BET surface area (112.0 m^2/g), shows a broad but weak peak around 800 Å, indicative of macropores. While macropores contribute to overall surface area, they are less effective for photocatalysis because they reduce the probability of reactant molecules interacting with active sites. Dong, Yang, ullah, irshad and Xue [68] similarly reported that excessive g-C_3N_4 loading can lead to structural irregularities and macropore formation, which compromise pore uniformity and catalytic efficiency. Ni/Mg/CN10, on the other hand, suffers from reduced surface area and irregular pore widening, likely due to partial pore blockage at low CN loading.

3.5. FT-IR Analysis

Understanding the characteristic absorption peaks of nickel oxide–magnesium oxide composites and carbon nitride in FT-IR analysis is crucial for identifying their structures. Figure 5 presents the FT-IR analysis of the composite nickel oxide (NiO) and magnesium oxide (MgO), which are both metal oxides with infrared characteristic peaks that primarily originate from the stretching vibrations of metal–oxygen bonds (M–O). The Ni–O stretching vibration typically exhibits a broad or intense absorption peak in the range of 500–700 cm^{-1} [72,73], constituting the primary characteristic peak of NiO. Its precise position and shape are influenced by nanoparticle size, crystallinity, and the method of complexation with magnesium oxide. On the other hand, the absorption peak for Mg-O bond stretching typically appears below 870 cm^{-1}, and it may even occur below 500 cm^{-1} [74]. Because of its relatively low intensity and overlap with the Ni–O peak, this band is often difficult to resolve individually in composite materials, frequently appearing as part of a broad composite peak. In addition, the composite surface readily adsorbs water or generates hydroxyl groups, which gives rise to a broad and intense O–H stretching vibration observed in the ~3700–3200 cm^{-1} region [75]. In addition to the broad O–H stretching vibration observed in the ~3700–3200 cm^{-1} region, a bending vibration peak for H–O–H may also appear near ~1630 cm^{-1}, which is typically attributed to adsorbed water molecules. When exposed to air, the material surface can readily adsorb CO_2, resulting in the formation of carbonate species. These are often detected as smaller peaks in the ~1500–1300 cm^{-1} region, corresponding to C–O stretching vibrations, and in the ~1000–800 cm^{-1} region, associated with carbonate bending modes. Such features are commonly reported in the FTIR spectra of oxide-based and g-C_3N_4 composites, where surface hydroxyls and adsorbed carbonates contribute to broad, overlapping bands that complicate spectral resolution [63,68].

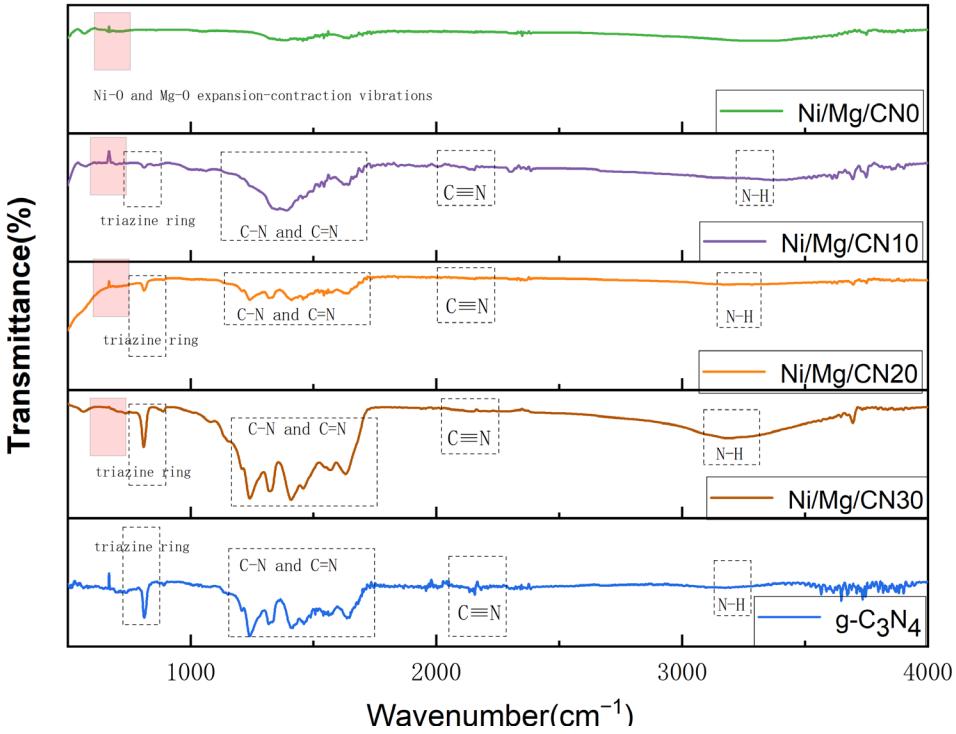

Figure 5. Fourier transform infrared absorption spectroscopy of the catalyst.

A series of sharp or split multiple absorption peaks typically appear within the 1200–1700 cm^{-1} region, which are characteristic of the aromatic C–N heterocyclic skeleton of g-C_3N_4. For example, common peak positions include ~1640 cm^{-1} (C=N stretching), ~1560 cm^{-1}, ~1460 cm^{-1}, ~1410 cm^{-1}, and ~1320 cm^{-1}, all of which correspond to the

stretching vibrations of the conjugated C–N framework. The out-of-plane breathing vibrations of the triazine ring typically exhibit a strong, sharp characteristic peak near 800–890 cm^{-1} (commonly ~805 cm^{-1}) [76], representing one of the most distinctive signatures of g-C_3N_4. Due to incomplete condensation during synthesis, g-C_3N_4 edges often retain -NH_2 or =NH groups, manifesting as weak to moderate peaks in the 3000–3300 cm^{-1} region [77]. In certain carbon nitride materials or at defect sites, a sharp peak may appear near ~2170 cm^{-1}. This is typically attributed to the stretching vibration of the cyano group (C≡N) [78].

In pure g-C_3N_4, the characteristic C–N and C=N stretching vibrations between 1200 and 1700 cm^{-1} and the distinct triazine ring breathing mode near 805 cm^{-1} appear to be sharp and intense [76], indicating a well-preserved conjugated framework. After the introduction of NiO [74] and MgO, these characteristic bands become weaker and slightly shift toward higher wavenumbers, implying that the electronic density around the nitrogen sites is altered through coordination or electrostatic interaction with Ni^{2+} and Mg^{2+} cations. Meanwhile, the broad O–H stretching vibration (3700–3200 cm^{-1}) and H–O–H bending mode (~1630 cm^{-1}) are more pronounced in the composites than in the individual oxides, suggesting increased surface hydroxylation or adsorbed moisture associated with the oxide support. In addition, the Mg–O stretching region (500–700 cm^{-1}) becomes broader and less symmetric in the composite, indicating overlapping contributions from Ni–O and Mg–O vibrations and possible lattice distortion at the interface. To more intuitively compare the structural characteristics and interactions of the various materials, Table 2 lists the FTIR characteristic peak assignments of the composite materials.

Table 2. Comparison of FT-IR characteristic absorption peaks of the catalyst.

Catalyst	Wavenumbers (cm^{-1})	Vibrational
g-C_3N_4	~805 (800–890)	Triazine ring out-of-plane breathing
	1200–1700	Aromatic C–N/C=N stretching
	3000–3300	Stretching of terminal –NH_2 or =NH
	~2170	C≡N stretching
Ni/Mg	500–700	Ni–O, Mg–O stretching
	<500	Mg–O bond stretching
Composites	3200–3700	O–H stretching
	~1630	H–O–H bending
	1300–1500, 800–1000	C–O stretching/bending (Carbonates)

Taken together, these spectral variations collectively confirm that the components are not merely physically mixed but are chemically coupled through N–metal coordination and hydrogen bonding. The modified vibration features provide solid evidence for the successful formation of the Ni–Mg/g-C_3N_4 heterojunction and the establishment of strong interfacial interactions that facilitate charge transfer during photocatalysis, consistent with previous reports on g-C_3N_4-based composites [63,68,79,80].

3.6. TGA Analysis

As shown in Figure 6, thermogravimetric analysis (TGA) shows that increasing the wt% of g-C_3N_4 in the Ni–Mg composites results in greater weight dissipation at ~550 °C, which reflects the progressive thermal decomposition of the g-C_3N_4 framework. A sharp decrease in weight loss is also observed for all CN-incorporated samples at ~200–220 °C, dropping by ~5 wt%, a feature commonly attributed to the removal of adsorbed water

and volatile surface groups such as hydroxyls and carbonates. This behavior is consistent with reports on g-C_3N_4 and Ni/Mg oxide composites, where early mass loss corresponds to dehydration and degassing rather than structural effects [63,79,80]. In contrast, pure NiO and pure MgO typically exhibit negligible weight loss below 800 °C, reflecting their high thermal stability and the absence of organic moieties; only minor mass changes are observed due to surface hydroxyl removal or oxygen vacancy adjustments [81,82].

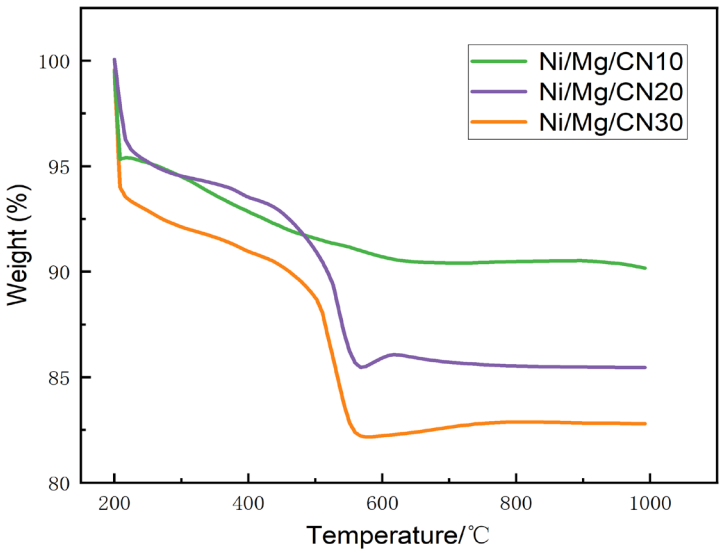

Figure 6. Thermogravimetric analysis (TGA) of the catalyst.

The final residual weights of ~90+% for Ni/Mg/CN10, ~85 wt% for Ni/Mg/CN20, and ~82.5 wt% for Ni/Mg/CN30 indicate that higher CN loading reduces the relative thermal stability of the composite, leaving less inorganic residue after heating. This trend suggests that while Ni–Mg oxides contribute to structural stability, increasing CN content introduces more organic polymeric material that decomposes upon heating. Similar reductions in residual mass with higher CN incorporation have been reported in other g-C_3N_4-based composites, where the balance between inorganic oxides and organic CN determines the char yield and influences material robustness [71,83]. The TGA curves reflect the surface cleanliness and structural stability of the material. Weight loss below 200 °C ensures the exposure of active sites, while stability below 500 °C guarantees the skeletal integrity of the composite material under actual operating conditions, which is a prerequisite for maintaining high catalytic activity [82]. Specifically, thermal stability ensures the durability of the heterojunction interface between g-C_3N_4 and NiO/MgO [84], thereby achieving the continuous and efficient separation of photogenerated carriers [85]. In this context, the composite with Ni/Mg/CN30 exhibited more pronounced decomposition at ca. 500 °C compared to Ni/Mg/CN20, suggesting lower skeletal integrity. By contrast, the enhanced thermal stability of Ni/Mg/CN20 preserves the g-C_3N_4/NiO/MgO heterojunction and active-site architecture [84], thereby promoting more efficient charge separation and ultimately resulting in superior catalytic performance [85].

3.7. Analysis of Photocatalytic Performance

Compared to studies using pure g-C_3N_4 as a photocatalyst [86], which typically suffer from limited visible-light absorption and rapid electron–hole recombination, the introduction of transition metal species (e.g., Ni) or metal oxides has been widely demonstrated to enhance activity by improving charge separation and introducing additional active sites [87,88]. Pure g-C_3N_4, as a baseline material, generally exhibits moderate degradation of organic dyes under visible-light irradiation, but the reaction rate constant is significantly

increased after metal doping or coupling. Ni-containing modifications (Ni doping, Ni clusters, or NiO hybrids) primarily accelerate charge transfer by acting as electron traps or forming heterojunctions, thereby improving photocatalytic performance; this mechanism is generally attributed to the following: enhanced separation of photogenerated carriers through nickel-related states or metal-semiconductor contacts [89] and increased reaction sites on the surface of nickel species. Meanwhile, MgO modifications of g-C_3N_4 offer complementary advantages [90]: MgO can enhance the adsorption capacity of both alkaline and acidic pollutants on the surface [91,92], inhibit recombination through the formation of heterojunctions, and sometimes improve the dispersion/exfoliation of the g-C_3N_4 layer, thereby increasing its activity in pollutant degradation [56]. However, MgO itself has relatively low visible light activity; thus, its effects are mainly manifested in structural and interfacial aspects rather than adding new photoexcitation pathways.

Figure 7 shows the changes in the photocatalytic degradation efficiency of all catalysts over time. To begin, a control experiment showed that there was an insignificant reduction in the MB degradation in the absence of any composites. The photodegradation of MB by g-C_3N_4 proceeds through two complementary processes: adsorption in the dark phase and photocatalysis under visible-light irradiation. During the initial dark phase, ~11% of MB was removed, which can be attributed to the high specific surface area and porous structure of g-C_3N_4, as well as its abundant nitrogen functionalities (–NH_2 and –OH) that promote dye adsorption. This adsorption step is crucial because it concentrates dye molecules at the catalyst surface, enhancing their accessibility for subsequent photocatalytic reactions. For context, the literature reports bandgap values of ~3.6–4.0 eV for NiO, ~7.8 eV for MgO, and ~2.7 eV for g-C_3N_4, indicating that the incorporation of CN into Ni/Mg oxides effectively narrows the overall bandgap and extends visible-light absorption [93,94]. The photogenerated electrons in the conduction band reduce O_2 to superoxide radicals ($\bullet O_2^-$), while holes in the valence band oxidize water or hydroxyl groups to produce hydroxyl radicals (•OH). These reactive oxygen species attack the aromatic rings and chromophoric groups of MB, resulting in decolorization and eventual mineralization. Similar two-step behavior, whereby the adsorption was followed by photocatalytic degradation, has been widely reported in g-C_3N_4-based composites, where adsorption enhances dye–catalyst contact and heterojunction formation with metals such as Ni or Mg, further improving charge separation and photocatalytic efficiency [63,68,79,80]. Thus, the observed 11% adsorption efficiency in the dark phase and subsequent photocatalytic degradation under visible light confirm the dual role of g-C_3N_4 as both an adsorbent and a photocatalyst.

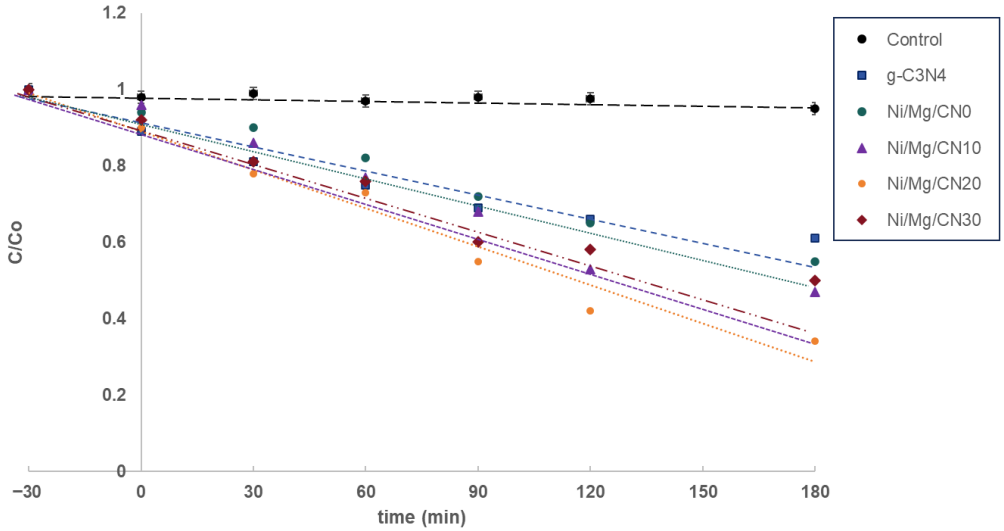

Figure 7. Photocatalytic performance result of composite percentage removal.

In contrast, Ni/Mg-O alone showed weak adsorption and limited photocatalytic activity, confirming that dye removal in the absence of light is primarily attributed to the CN framework rather than the oxide. Notably, varying CN loadings produced different outcomes, with Ni/Mg/CN20 exhibiting the highest degradation (~66% at 180 min). This optimum performance can be explained by the characterization results: FTIR confirmed N–metal coordination and hydrogen bonding indicative of heterojunction formation, TGA revealed a balanced organic/inorganic composition, and pore size distribution showed that CN20 possessed mesopores in the 80–150 Å range, which the literature identifies as particularly favourable for photocatalysis [71,83]. By comparison, CN10 lacked sufficient CN to establish effective heterojunctions, while CN30 introduced excess CN that disrupted oxide dispersion and shifted porosity toward macropores, resulting in higher charge recombination.

Similar patterns—low performance of single components and enhanced activity in g-C_3N_4–oxide composites—are reported for the g-C_3N_4/$NiCuFe_2O_4$ and g-C_3N_4/ZnO systems, where coupling improves charge separation and drives higher MB degradation than either constituent alone [95,96]. The superior performance of Ni/Mg/CN20, therefore, highlights the significance of optimizing CN incorporation to balance adsorption, charge transfer, and pore structure, a principle broadly recognized in g-C_3N_4-based heterojunctions for environmental remediation [63,79,80].

4. Further Discussion

To elucidate the reaction mechanism, Figure 8 demonstrates that the photocatalytic degradation of methylene blue (MB) over the Ni/Mg/g-C_3N_4 composite follows a direct Z-scheme charge transfer mechanism. Under visible-light irradiation, both g-C_3N_4 and NiO–MgO are photoexcited to generate electron–hole pairs. At the heterojunction interface, the photogenerated electrons in the conduction band (CB) of NiO–MgO recombine with holes in the valence band (VB) of g-C_3N_4. This recombination pathway preserves the spatial separation of the more energetic charge carriers: electrons in the CB of g-C_3N_4 and holes in the VB of NiO–MgO. Such separation maintains strong redox potentials, enabling efficient photocatalysis [97–99].

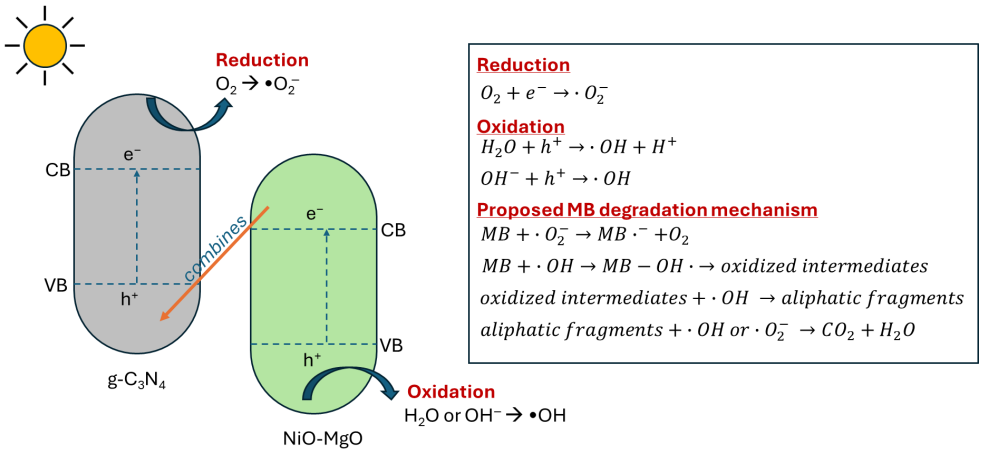

Figure 8. Schematic diagram of reaction mechanism.

In this configuration, the conduction band (CB) electrons of g-C_3N_4 reduce adsorbed O_2 to superoxide radicals ($\bullet O_2^-$), while the VB holes of NiO–MgO oxidize surface H_2O or OH^- to hydroxyl radicals (•OH). These reactive oxygen species act synergistically to attack and mineralize MB molecules into CO_2 and H_2O. The presence of MgO enhances electron transfer and interfacial contact, improving charge mobility and junction stability [82]. NiO

contributes to visible-light absorption and facilitates charge separation by red-shifting the absorption edge of g-C_3N_4 and promoting carrier migration [84]. Together, the Ni/Mg/g-C_3N_4 heterostructure effectively suppresses charge recombination and promotes a robust oxidation–reduction cycle, resulting in markedly improved degradation efficiency compared to the individual components. This Z-scheme mechanism has been widely validated in similar systems, including g-C_3N_4/NiO/ZnO and g-C_3N_4/MgO composites, where the spatial separation of charge carriers and strong redox potentials were key to enhanced photocatalytic performance [85].

Similar Z-scheme behavior has been widely reported in g-C_3N_4-based composites. Oxygen-doped g-C_3N_4/NiS systems demonstrated enhanced dye degradation due to efficient charge separation and ROS generation [79]. g-C_3N_4/ZnO nanocomposites showed superior MB removal under visible light, attributed to Z-scheme electron transfer that preserved strong redox potentials [96]. $NiCuFe_2O_4$/g-C_3N_4 composites also exhibited improved MB degradation efficiency compared to single components, confirming that heterojunction formation is critical for suppressing recombination and enhancing ROS production [95]. Likewise, Mg–Al LDH@g-C_3N_4 composites performed significantly better than LDH alone, further validating the role of CN interfaces in boosting photocatalysis [100,101].

Thus, the Ni/Mg/g-C_3N_4 composite not only demonstrates the classical advantages of Z-scheme heterojunctions, which possess strong redox ability and suppressed recombination, but also highlights the synergistic contributions of MgO (electron transfer and interfacial contact) and NiO (visible-light absorption and charge separation). This outcome is significant because it establishes Ni/Mg/g-C_3N_4 as a promising photocatalyst for environmental remediation, aligning with broader trends in g-C_3N_4-based heterostructures where optimized interfaces drive superior pollutant degradation.

The optimum performance observed for Ni/Mg/CN20 can be explained by a combination of structural, electronic, and interfacial factors. At ~20 wt% CN, the composite achieves a critical balance: CN domains are sufficiently abundant for forming continuous electron pathways across the NiO–MgO surface yet not so excessive as to cause agglomeration or block oxide active sites. This "percolation threshold" ensures maximum heterojunction density and efficient charge transfer [102,103]. At lower loadings (CN10), CN coverage is too sparse to establish continuous junctions, while higher loadings (CN30) lead to CN stacking, which reduces accessible surface area and creates "self-shielding" effects that hinder photon penetration.

The pore structure plays a decisive role in this balance. Ni/Mg/CN20 maintains mesopores in the 80–150 Å range, which are widely recognized as optimal for photocatalysis because they provide high surface area while allowing the rapid diffusion of dye molecules and reactive oxygen species [61]. Ni/Mg/CN30, however, shifts toward macropores, which reduces adsorption efficiency and slows diffusion kinetics. The hierarchical porosity of NiO–MgO combined with CN layers at 20 wt% creates a synergistic architecture: micropores trap MB molecules, mesopores accelerate transport, and surface roughness increases active site exposure.

The composite synergy further enhances photocatalysis. NiO contributes visible-light absorption, MgO improves electron mobility and interfacial contact, and CN acts as a mediator bridging both oxides. At 20% CN, this tri-component interaction is maximized, reinforcing the direct Z-scheme mechanism and ensuring the simultaneous generation of superoxide ($\bullet O_2^-$) and hydroxyl radicals (•OH). This dual ROS production is less efficient in CN10 (weak heterojunction formation) and CN30 (blocked diffusion and recombination) [61,85,87].

From a mechanistic perspective, the formation of p–n or n–n heterojunctions between semiconducting components provides an internal electric field that drives the directional

migration of charge carriers. At the NiO–MgO/g-C_3N_4 interface, photogenerated electrons in the CB of NiO–MgO recombine with holes in the VB of g-C_3N_4, while the more energetic carriers (CB electrons in g-C_3N_4 and VB holes in NiO–MgO) are preserved. This spatial separation maintains strong redox potentials, enabling efficient ROS generation and MB mineralization. Such mechanisms align with previous studies on multi-component heterostructures, where rational band alignment optimized charge separation and light absorption [97–99].

Other studies support these findings. For example, g-C_3N_4/ZnO nanocomposites showed maximum MB degradation at ~20 wt% CN, attributed to a balanced heterojunction density and mesoporous structure [96]. $NiCuFe_2O_4$/g-C_3N_4 composites also demonstrated enhanced MB degradation compared to single components, confirming that CN interfaces are critical for suppressing recombination [95]. Similarly, Mg–Al LDH@g-C_3N_4 composites outperformed LDH alone, validating the role of CN in boosting [100]. Reviews by Zhang, Lian, Hao, Zhang, Yang, Jiang, Zhang, Liao and Qin [101] and Ahmed, Mahmoud and Mohamed [64] further emphasize that CN modification strategies—including doping, exfoliation, and heterojunction formation—are key to maximizing photocatalytic efficiency. On the other hand, similar observations were also observed on perovskite composites, where interface engineering was shown to dramatically enhance charge transfer and catalytic activity [104].

Although the Ni/Mg/g-C_3N_4 composite demonstrates efficient photocatalytic degradation of MB via a direct Z-scheme mechanism, the absolute degradation rate is not markedly superior to those reported in prior studies. This outcome can be rationalized by several structural and mechanistic factors. First, while the incorporation of g-C_3N_4 enhances heterojunction formation, the BET surface area and pore architecture of the composite remain within the typical range of g-C_3N_4/oxide systems, meaning that the density of accessible active sites is not dramatically increased [82]. Second, although the Z-scheme interface facilitates charge separation, the suppression of electron–hole recombination may be moderate compared to systems incorporating additional dopants or co-catalysts, which have been shown to further accelerate carrier migration [84]. Third, the optical absorption edge of the composite remains close to that of pristine g-C_3N_4, limiting visible-light harvesting and thereby constraining photocatalytic efficiency [85]. Finally, our experimental conditions were optimized to highlight reproducibility and structural stability rather than maximize absolute degradation rates, which may explain the modest improvement observed. Importantly, the enhanced stability of Ni/Mg/CN20 ensures skeletal integrity and heterojunction durability, enabling sustained catalytic activity and reusability, which recent reviews emphasize as equally critical to practical photocatalytic applications [85]. Thus, while the rate enhancement is moderate, the Ni/Mg/CN system provides a valuable balance of activity, durability, and mechanistic clarity, positioning it as a promising candidate for long-term environmental remediation.

In a broader context, this study provides a feasible strategy for designing efficient, low-cost, and environmentally benign photocatalysts for dye degradation and other remediation applications. Future research may focus on finetuning the Ni/Mg ratio to optimize band alignment, controlling calcination conditions to tailor porosity and crystallinity, and evaluating performance under natural sunlight or in real wastewater systems. Moreover, coupling this heterostructure with plasmonic nanoparticles (Ag, Au) or carbon-based materials (graphene and CNTs) could further expand light absorption, accelerate electron transport, and improve stability. Such strategies open new avenues for scalable photocatalytic technologies, positioning CN-based heterostructures as promising candidates for sustainable wastewater treatment and environmental remediation.

5. Conclusions

This study successfully demonstrates the incorporation of ternary Ni/Mg/g-C_3N_4 composites, which enhance photocatalytic performance through synergistic structural and electronic interactions. The integration of NiO, MgO, and g-C_3N_4 establishes effective heterojunctions, improves charge separation, and reinforces Z-scheme pathways, resulting in the efficient generation of reactive oxygen species. Among all samples, Ni/Mg/CN20 exhibited the highest activity, achieving 66% MB degradation within 180 min under visible light, a performance attributed to broadened light absorption, efficient interfacial charge transfer, and abundant active sites. The composite also displayed excellent thermal stability, with TGA confirming that the rational control of g-C_3N_4 loading directly influences porosity, skeletal integrity, and char yield.

The novelty of this work lies in identifying the optimum CN incorporation that maximizes heterojunction density while maintaining mesoporous architecture, a mechanistic insight not previously reported in the literature. This achievement offers a new design principle for g-C_3N_4-based composites, demonstrating that the rational tuning of component ratios and pore structures can significantly boost photocatalytic efficiency while preserving structural robustness.

Overall, the successful construction of Ni/Mg/CN20 highlights a scalable and environmentally benign strategy for advanced photocatalytic applications. Beyond dye degradation, the insights gained here provide a foundation for extending Ni/Mg/g-C_3N_4 composites to hydrogen evolution, carbon dioxide reduction, and real wastewater treatment, thereby advancing the development of cost-effective and durable photocatalysts for sustainable environmental remediation.

Author Contributions: Conceptualization, S.H. and T.J.T.; methodology, S.H. and S.W.C.; validation, S.H. and T.J.T.; investigation, S.H. and S.W.C.; data curation, S.H. and S.W.C.; writing—original draft preparation, S.H. and Y.H.Y.; writing—review and editing, Y.H.Y. and T.J.T.; visualization, S.H.; supervision, T.J.T. and C.-M.H.; project administration, T.J.T. and C.-M.H.; funding acquisition, C.-M.H. All authors have read and agreed to the published version of the manuscript.

Funding: This research was funded by the Ministry of Higher Education of Malaysia via the Fundamentals Research Grant Scheme (FRGS/1/2023/STG04/UNIM/02/1) and the National Science and Technology Council (NSTC) of Taiwan under project NSTC 113-2637-E-168-002.

Data Availability Statement: The original contributions presented in this study are included in the article. Further inquiries can be directed to the corresponding author.

Conflicts of Interest: The authors declare no conflicts of interest.

References

1. Alegbe, E.O.; Uthman, T.O. A review of history, properties, classification, applications and challenges of natural and synthetic dyes. *Heliyon* **2024**, *10*, e33646. [CrossRef]
2. Benkhaya, S.; M' rabet, S.; El Harfi, A. A review on classifications, recent synthesis and applications of textile dyes. *Inorg. Chem. Commun.* **2020**, *115*, 107891. [CrossRef]
3. Al-Tohamy, R.; Ali, S.S.; Li, F.; Okasha, K.M.; Mahmoud, Y.A.G.; Elsamahy, T.; Jiao, H.; Fu, Y.; Sun, J. A critical review on the treatment of dye-containing wastewater: Ecotoxicological and health concerns of textile dyes and possible remediation approaches for environmental safety. *Ecotoxicol. Environ. Saf.* **2022**, *231*, 113160. [CrossRef]
4. Tkaczyk, A.; Mitrowska, K.; Posyniak, A. Synthetic organic dyes as contaminants of the aquatic environment and their implications for ecosystems: A review. *Sci. Total Environ.* **2020**, *717*, 137222. [CrossRef]
5. Kamati, S.N.; Yan, J.; Fan, J. A review on progresses in reactive dye-containing wastewater treatment. *Water Pract. Technol.* **2024**, *19*, 2712–2733. [CrossRef]
6. Ewuzie, U.; Saliu, O.D.; Dulta, K.; Ogunniyi, S.; Bajeh, A.O.; Iwuozor, K.O.; Ighalo, J.O. A review on treatment technologies for printing and dyeing wastewater (PDW). *J. Water Process Eng.* **2022**, *50*, 103273. [CrossRef]

7. Sharma, J.; Sharma, S.; Soni, V. Classification and impact of synthetic textile dyes on Aquatic Flora: A review. *Reg. Stud. Mar. Sci.* **2021**, *45*, 101802. [CrossRef]
8. Krishna Moorthy, A.; Govindarajan Rathi, B.; Shukla, S.P.; Kumar, K.; Shree Bharti, V. Acute toxicity of textile dye Methylene blue on growth and metabolism of selected freshwater microalgae. *Environ. Toxicol. Pharmacol.* **2021**, *82*, 103552. [CrossRef]
9. Khodaie, M.; Ghasemi, N.; Moradi, B.; Rahimi, M. Removal of Methylene Blue from Wastewater by Adsorption onto ZnCl2 Activated Corn Husk Carbon Equilibrium Studies. *J. Chem.* **2013**, *2013*, 383985. [CrossRef]
10. Dardouri, S.; Sghaier, J. Adsorptive removal of methylene blue from aqueous solution using different agricultural wastes as adsorbents. *Korean J. Chem.* **2017**, *34*, 1037–1043. [CrossRef]
11. Ginimuge, P.R.; Jyothi, S.D. Methylene Blue: Revisited. *J. Anaesthesiol. Clin. Pharmacol.* **2010**, *26*, 517–520. [CrossRef]
12. Meissner, P.E.; Mandi, G.; Coulibaly, B.; Witte, S.; Tapsoba, T.; Mansmann, U.; Rengelshausen, J.; Schiek, W.; Jahn, A.; Walter-Sack, I.; et al. Methylene blue for malaria in Africa: Results from a dose-finding study in combination with chloroquine. *Malar. J.* **2006**, *5*, 84. [CrossRef]
13. Oladoye, P.O.; Ajiboye, T.O.; Omotola, E.O.; Oyewola, O.J. Methylene blue dye: Toxicity and potential elimination technology from wastewater. *Results Eng.* **2022**, *16*, 100678. [CrossRef]
14. Elewa, K.; Tawfic, A.F.; Tarek, M.; Al-Sagheer, N.A.; Nagy, N.M. Removal of methylene blue from synthetic industrial wastewater by using geopolymer prepared from partially dealuminated metakaolin. *Sci. Rep.* **2025**, *15*, 17633. [CrossRef]
15. Appia, F.T.A.; Kouassi, T.G.D.; Kimou, K.J.; Coulibaly, C.S.; Meledje, J.-C.; Ouattara, L. Photolytic Degradation of Methylene Blue: The Effect of Various Factors on Wastewater Treatment Efficiency. *Asian J. Chem. Sci.* **2025**, *15*, 41–52. [CrossRef]
16. Kuspanov, Z.; Bakbolat, B.; Baimenov, A.; Issadykov, A.; Yeleuov, M.; Daulbayev, C. Photocatalysts for a sustainable future: Innovations in large-scale environmental and energy applications. *Sci. Total Environ.* **2023**, *885*, 163914. [CrossRef] [PubMed]
17. Chen, K.; Dong, W.; Huang, Y.; Wang, F.; Zhou, J.L.; Li, W. Photocatalysis for sustainable energy and environmental protection in construction: A review on surface engineering and emerging synthesis. *J. Environ. Chem. Eng.* **2025**, *13*, 117529. [CrossRef]
18. Majeed, A.; Iqbal, M.A.; Do, T.-O. Advances in Composite Photocatalysts for Efficient Degradation of Organic Pollutants: Strategies, Challenges, and Future Perspectives. *Catalysts* **2025**, *15*, 893. [CrossRef]
19. Li, J.; Guan, L.; Jiang, L.; Xu, M.; Li, J.; Zuo, J.; Tan, C.; Xia, Z. Construction of 2D/3D g-C_3N_4/BiOI Photocatalysts with p-n Heterojunction and Their Performance in Photocatalytic Degradation of Amaranth Dye. *ACS Omega* **2024**, *9*, 361–370. [CrossRef]
20. Chen, C.-Y.; Tseng, C.-C. Two-dimensional Ga2S3/g-C_3N_4 heterojunction composites with highly enhanced photocatalytic activity and stability. *Adv. Compos. Hybrid Mater.* **2022**, *6*, 20. [CrossRef]
21. Mahmoudi, F.; Bachas, L.G. Application of Metal–Organic Framework-Based Composite Materials for Photodegradation of Dye Pollutants in Wastewater. *Water* **2024**, *16*, 3051. [CrossRef]
22. Marchi, M.; Gentile, G.; Rosso, C.; Melchionna, M.; Fornasiero, P.; Filippini, G.; Prato, M. The Nickel Age in Synthetic Dual Photocatalysis: A Bright Trip Toward Materials Science. *ChemSusChem* **2022**, *15*, e202201094. [CrossRef]
23. Ling, B.; Yao, S.; Ouyang, S.; Bai, H.; Zhai, X.; Zhu, C.; Li, W.; Xie, J. Nickel-Catalyzed Highly Selective Radical C−C Coupling from Carboxylic Acids with Photoredox Catalysis. *Angew. Chem. Int. Ed.* **2024**, *63*, e202405866. [CrossRef]
24. Chen, W.-T.; Chan, A.; Sun-Waterhouse, D.; Moriga, T.; Idriss, H.; Waterhouse, G.I.N. Ni/TiO2: A promising low-cost photocatalytic system for solar H2 production from ethanol–water mixtures. *J. Catal.* **2015**, *326*, 43–53. [CrossRef]
25. Zou, M.; Feng, L.; Ganeshraja, A.S.; Xiong, F.; Yang, M. Defect induced nickel, nitrogen-codoped mesoporous TiO2 microspheres with enhanced visible light photocatalytic activity. *Solid State Sci.* **2016**, *60*, 1–10. [CrossRef]
26. Bi, L.; Xu, D.; Zhang, L.; Lin, Y.; Wang, D.; Xie, T. Metal Ni-loaded gC_3N_4 for enhanced photocatalytic H_2 evolution activity: The change in surface band bending. *Phys. Chem. Chem. Phys.* **2015**, *17*, 29899–29905. [CrossRef] [PubMed]
27. Pieta, I.S.; Gieroba, B.; Kalisz, G.; Pieta, P.; Nowakowski, R.; Naushad, M.; Rathi, A.; Gawande, M.B.; Sroka-Bartnicka, A.; Zboril, R. Developing Benign Ni/g-C_3N_4 Catalysts for CO2 Hydrogenation: Activity and Toxicity Study. *Ind. Eng. Chem. Res.* **2022**, *61*, 10496–10510. [CrossRef] [PubMed]
28. Qi, Z.-H.; Ma, J. Dual Role of a Photocatalyst: Generation of Ni(0) Catalyst and Promotion of Catalytic C–N Bond Formation. *ACS Catal.* **2018**, *8*, 1456–1463. [CrossRef]
29. Kamal, K.M.; Narayan, R.; Periasamy, S.; Gyergyek, S.; Popović, S.; Hodnik, N.; Ho, H.-C.; Djinović, P.; Likozar, B. Precise design and construction of NiO-Ni heterostructures for active hydrogen evolution photocatalysis. *Appl. Catal. O Open* **2024**, *194*, 206997. [CrossRef]
30. Sun, B.; Zhou, G.; Gao, T.; Zhang, H.; Yu, H. NiO nanosheet/TiO2 nanorod-constructed p–n heterostructures for improved photocatalytic activity. *Appl. Surf. Sci.* **2016**, *364*, 322–331. [CrossRef]
31. Yu, C.; Li, M.; Yang, D.; Pan, K.; Yang, F.; Xu, Y.; Yuan, L.; Qu, Y.; Zhou, W. NiO nanoparticles dotted TiO2 nanosheets assembled nanotubes P-N heterojunctions for efficient interface charge separation and photocatalytic hydrogen evolution. *Appl. Surf. Sci.* **2021**, *568*, 150981. [CrossRef]
32. Xia, Q.X.; Hui, K.S.; Hui, K.N.; Hwang, D.H.; Lee, S.K.; Zhou, W.; Cho, Y.R.; Kwon, S.H.; Wang, Q.M.; Son, Y.G. A facile synthesis method of hierarchically porous NiO nanosheets. *Mater. Lett.* **2012**, *69*, 69–71. [CrossRef]

33. Mollamahale, Y.B.; Liu, Z.; Zhen, Y.; Tian, Z.Q.; Hosseini, D.; Chen, L.; Shen, P.K. Simple fabrication of porous NiO nanoflowers: Growth mechanism, shape evolution and their application into Li-ion batteries. *Int. J. Hydrogen Energy* **2017**, *42*, 7202–7211. [CrossRef]
34. Yu, W.; Jiang, X.; Ding, S.; Li, B.Q. Preparation and electrochemical characteristics of porous hollow spheres of NiO nanosheets as electrodes of supercapacitors. *J. Power Sources* **2014**, *256*, 440–448. [CrossRef]
35. Du, R.; Xiao, K.; Li, B.; Han, X.; Zhang, C.; Wang, X.; Zuo, Y.; Guardia, P.; Li, J.; Chen, J.; et al. Controlled oxygen doping in highly dispersed Ni-loaded g-C_3N_4 nanotubes for efficient photocatalytic H2O2 production. *Chem. Eng. J.* **2022**, *441*, 135999. [CrossRef]
36. Ai, L.; Zeng, Y. Hierarchical porous NiO architectures as highly recyclable adsorbents for effective removal of organic dye from aqueous solution. *Chem. Eng. J.* **2013**, *215-216*, 269–278. [CrossRef]
37. Song, Z.; Chen, L.; Hu, J.; Richards, R. NiO(111) nanosheets as efficient and recyclable adsorbents for dye pollutant removal from wastewater. *Nanotechnology* **2009**, *20*, 275707. [CrossRef] [PubMed]
38. Chinthala, M.; Balakrishnan, A.; Venkataraman, P.; Manaswini Gowtham, V.; Polagani, R.K. Synthesis and applications of nano-MgO and composites for medicine, energy, and environmental remediation: A review. *Environ. Chem. Lett.* **2021**, *19*, 4415–4454. [CrossRef]
39. He, Y.; Li, Z.; Xue, M.; Qi, X.; Li, J.; Jiang, K.; Fu, J.; Guan, C.; Sun, K.; Shi, Z.; et al. Enhanced adsorption performance of subordinate magnesium sites in pinhole magnesium oxide nanosheets with rich oxygen vacancies. *Environ. Funct. Mater.* **2022**, *1*, 105–113. [CrossRef]
40. Julkapli, N.M.; Bagheri, S. Magnesium oxide as a heterogeneous catalyst support. *Rev. Inorg. Chem.* **2016**, *36*, 1–41. [CrossRef]
41. Li, Q.; Zong, L.; Li, C.; Yang, J. Reprint of "Photocatalytic reduction of CO2 on MgO/TiO2 nanotube films". *Appl. Surf. Sci.* **2014**, *319*, 16–20. [CrossRef]
42. Nigam, A.; Saini, S.; Rai, A.K.; Pawar, S.J. Structural, optical, cytotoxicity, and antimicrobial properties of MgO, ZnO and MgO/ZnO nanocomposite for biomedical applications. *Ceram. Int.* **2021**, *47*, 19515–19525. [CrossRef]
43. Allawi, F.; Juda, A.M.; Radhi, S.W. Photocatalytic degradation of methylene blue over MgO/α-Fe2O3 nano composite prepared by a hydrothermal method. *AIP Conf. Proc.* **2020**, *2290*, 030020. [CrossRef]
44. Baysal, T.; Noor, N.; Demir, A. Nanofibrous MgO composites: Structures, properties, and applications. *Polym.-Plast. Technol. Mater.* **2020**, *59*, 1522–1551. [CrossRef]
45. Chauhan, D.; Kumar, R.; Thakur, N.; Kumar, K. Exploring transition metal (Co, Cu, and Zn) doped magnesium oxide nanoparticles for their environmental remediation potential. *Mater. Sci. Eng. B* **2024**, *302*, 117256. [CrossRef]
46. Zhang, C.; Fang, Z.; Cheng, H.; Jadhav, C.D.; Nie, J.; Liu, D.; Wang, Y.; Liang, Y. A novel NiO electrocatalyst with rich redox pairs and oxygen vacancies for methanol oxidation reaction: Mechanism and DFT study. *J. Alloys Compd.* **2025**, *1025*, 180184. [CrossRef]
47. Yang, L.; Jiao, Y.; Xu, X.; Pan, Y.; Su, C.; Duan, X.; Sun, H.; Liu, S.; Wang, S.; Shao, Z. Superstructures with Atomic-Level Arranged Perovskite and Oxide Layers for Advanced Oxidation with an Enhanced Non-Free Radical Pathway. *ACS Sustain. Chem. Eng.* **2022**, *10*, 1899–1909. [CrossRef]
48. Pathak, N.; Ghosh, P.S.; Gupta, S.K.; Kadam, R.M.; Arya, A. Defects induced changes in the electronic structures of MgO and their correlation with the optical properties: A special case of electron–hole recombination from the conduction band. *RSC Adv.* **2016**, *6*, 96398–96415. [CrossRef]
49. Fu, J.; Yu, J.; Jiang, C.; Cheng, B. g-C3N4-Based Heterostructured Photocatalysts. *Adv. Energy Mater.* **2018**, *8*, 1701503. [CrossRef]
50. Vaya, D.; Kaushik, B.; Surolia, P.K. Recent advances in graphitic carbon nitride semiconductor: Structure, synthesis and applications. *Mater. Sci. Semicond. Process.* **2022**, *137*, 106181. [CrossRef]
51. Sewnet, A.; Abebe, M.; Asaithambi, P.; Alemayehu, E. Visible-light-driven g-C_3N_4/TiO2 based heterojunction nanocomposites for photocatalytic degradation of organic dyes in wastewater: A review. *Air Soil Water Res.* **2022**, *15*. [CrossRef]
52. Tang, X.-C.; Ding, Z.; Wang, Z.-H.; Arif, N.; Chen, Y.-Y.; Li, L.; Zeng, Y.-J. Recent Advances in Photocatalytic Nitrogen Fixation Based on Two-Dimensional Materials. *ChemCatChem* **2024**, *16*, e202401355. [CrossRef]
53. Asghar, H.; Saeed, M.; Mirsafi, F.S.; Ismael, M.K.; Leißner, T.; Mishra, Y.K. Zinc Oxide-Graphitic Carbon Nitride Composites: Synthesis, Properties, and Application Scopes in Environmental Remediations. *Small* **2025**, *21*, e09637. [CrossRef]
54. Tahseen, T.; Farooq, N.; Iman, W.; Hareem, A.; Irshad, R.; Ibrahim, T.K.; Awadh Bahajjaj, A.A.; Manavalan, R.K.; Hussain, S. G-C3N4-based multi-metal oxide nanocomposites: A new frontier in catalytic performance. *Solid State Sci.* **2025**, *163*, 107890. [CrossRef]
55. Shi, J.-W.; Zou, Y.; Cheng, L.; Ma, D.; Sun, D.; Mao, S.; Sun, L.; He, C.; Wang, Z. In-situ phosphating to synthesize Ni2P decorated NiO/g-C_3N_4 p-n junction for enhanced photocatalytic hydrogen production. *Chem. Eng. J.* **2019**, *378*, 122161. [CrossRef]
56. Senevirathna, H.L.; Lee, W.P.C.; Wu, S.; Bai, K.; Wu, P. Facile synthesis of bandgap-engineered N-doped MgO/g-C3N4 nanocomposites for enhanced sunlight-driven photocatalytic degradation of organic dyes. *Mater. Chem. Phys.* **2025**, *332*, 130234. [CrossRef]
57. Gomaa, M.M.; Boshta, M.; Farag, B.S.; Osman, M.B.S. Structural and optical properties of nickel oxide thin films prepared by chemical bath deposition and by spray pyrolysis techniques. *J. Mater. Sci. Mater. Electron.* **2016**, *27*, 711–717. [CrossRef]

58. Yousefi, S.; Ghasemi, B. Precipitator concentration-dependent opto-structural properties of MgO nanoparticles fabricated using natural brine. *SN Appl. Sci.* **2020**, *2*, 852. [CrossRef]
59. Lin, B.; Li, H.; An, H.; Hao, W.; Wei, J.; Dai, Y.; Ma, C.; Yang, G. Preparation of 2D/2D g-C_3N_4 nanosheet@ZnIn2S4 nanoleaf heterojunctions with well-designed high-speed charge transfer nanochannels towards high-efficiency photocatalytic hydrogen evolution. *Appl. Catal. B Environ.* **2018**, *220*, 542–552. [CrossRef]
60. Zárate-Aguillón, A.; Navarro-Aguilar, A.I.; Ruiz-Gómez, M.A.; Obregón, S.; Vázquez, A. Improving electrophoretic deposition of (Mg/Al)-doped Ni(OH)2 through the generation of layered double hydroxides. *Appl. Phys. A* **2023**, *129*, 305. [CrossRef]
61. Jadhav, A.D.; Waghmode, J.V.; Sodmise, S.K.; Sapkal, R.T. Effect of Calcination Temperature on Synthesis of g-C_3N_4 and its Application in Photocatalytic degradation of Methylene Blue Dye. *Int. Res. J. Sci. Eng.* **2023**, 65–72. [CrossRef]
62. Al Mais, D.; Mustapha, S.; Baghdadi, Y.N.; Bouhadir, K.; Tehrani-Bagha, A.R. Various Morphologies of Graphitic Carbon Nitride (g-C_3N_4) and Their Effect on the Thermomechanical Properties of Thermoset Epoxy Resin Composites. *Polymers* **2024**, *16*, 1935. [CrossRef]
63. Shen, Q.; Wu, C.; You, Z.; Huang, F.; Sheng, J.; Zhang, F.; Cheng, D.; Yang, H. g-C_3N_4 nanoparticle@porous g-C_3N_4 composite photocatalytic materials with significantly enhanced photo-generated carrier separation efficiency. *J. Mater. Res.* **2020**, *35*, 2148–2157. [CrossRef]
64. Ahmed, M.A.; Mahmoud, S.A.; Mohamed, A.A. Unveiling the photocatalytic potential of graphitic carbon nitride (g-C_3N_4): A state-of-the-art review. *RSC Adv.* **2024**, *14*, 25629–25662. [CrossRef]
65. Liu, C.; Zhang, Y.; Dong, F.; Du, X.; Huang, H. Easily and Synchronously Ameliorating Charge Separation and Band Energy Level in Porous g-C_3N_4 for Boosting Photooxidation and Photoreduction Ability. *J. Phys. Chem. C* **2016**, *120*, 10381–10389. [CrossRef]
66. Li, J.; Zhang, Z.; Cui, W.; Wang, H.; Cen, W.; Johnson, G.; Jiang, G.; Zhang, S.; Dong, F. The Spatially Oriented Charge Flow and Photocatalysis Mechanism on Internal van der Waals Heterostructures Enhanced g-C3N4. *ACS Catal.* **2018**, *8*, 8376–8385. [CrossRef]
67. Xiong, T.; Cen, W.; Zhang, Y.; Dong, F. Bridging the g-C3N4 Interlayers for Enhanced Photocatalysis. *ACS Catal.* **2016**, *6*, 2462–2472. [CrossRef]
68. Dong, Z.; Yang, T.; ullah, I.; irshad, N.; Xue, S. The influence of morphological changes on the physicochemical and optical properties of g-C_3N_4. *Ceram. Int.* **2024**, *50*, 17882–17889. [CrossRef]
69. Banu, A.; Sinha, B.; Sikdar, S. Synthesis of polymeric 2D-graphitic carbon nitride (g-C_3N_4) nanosheets for sustainable photodegradation of organic pollutants. *Heliyon* **2024**, *10*, e33354. [CrossRef]
70. Durmus, Z.; Köferstein, R.; Lindenberg, T.; Lehmann, F.; Hinderberger, D.; Maijenburg, A.W. Preparation and characterization of Ce-MOF/g-C_3N_4 composites and evaluation of their photocatalytic performance. *Ceram. Int.* **2023**, *49*, 24428–24441. [CrossRef]
71. Yang, J.; Zhang, X.; Xie, C.; Long, J.; Wang, Y.; Wei, L.; Yang, X. Preparation of g-C3N4 with High Specific Surface Area and Photocatalytic Stability. *J. Electron. Mater.* **2021**, *50*, 1067–1074. [CrossRef]
72. Song, X.; Gao, L. Facile Synthesis and Hierarchical Assembly of Hollow Nickel Oxide Architectures Bearing Enhanced Photocatalytic Properties. *J. Phys. Chem. C* **2008**, *112*, 15299–15305. [CrossRef]
73. Volkov, V.V.; Wang, Z.L.; Zou, B.S. Carrier recombination in clusters of NiO. *Chem. Phys. Lett.* **2001**, *337*, 117–124. [CrossRef]
74. Dekermenjian, M.; Ruediger, A.P.; Merlen, A. Raman spectroscopy investigation of magnesium oxide nanoparticles. *RSC Adv.* **2023**, *13*, 26683–26689. [CrossRef] [PubMed]
75. Al-Senani, G.M.; Al-Fawzan, F.F.; Alshabanat, M.; Abd-Elkader, O.H.; Nasrallah, M.; Nasrallah, M. One Pot Synthesis, Surface, and Magnetic Properties of Ni–NiO@C Nanocomposites. *Crystals* **2023**, *13*, 1497. [CrossRef]
76. Wang, H.; He, W.; Dong, X.a.; Wang, H.; Dong, F. In situ FT-IR investigation on the reaction mechanism of visible light photocatalytic NO oxidation with defective g-C_3N_4. *Sci. Bull.* **2018**, *63*, 117–125. [CrossRef] [PubMed]
77. Boonprakob, N.; Wetchakun, N.; Phanichphant, S.; Waxler, D.; Sherrell, P.; Nattestad, A.; Chen, J.; Inceesungvorn, B. Enhanced visible-light photocatalytic activity of g-C_3N_4/TiO2 films. *J. Colloid. Interface Sci.* **2014**, *417*, 402–409. [CrossRef]
78. Yuan, X.; Luo, K.; Zhang, K.; He, J.; Zhao, Y.; Yu, D. Combinatorial Vibration-Mode Assignment for the FTIR Spectrum of Crystalline Melamine: A Strategic Approach toward Theoretical IR Vibrational Calculations of Triazine-Based Compounds. *J. Phys. Chem. A* **2016**, *120*, 7427–7433. [CrossRef]
79. Sarkar, N.; Gadore, V.; Mishra, S.R.; Ahmaruzzaman, M. Exploring Oxygen-Doped g-C_3N_4 Supported NiS Nanocomposites for Enhanced Photocatalytic Removal of Contaminants from Aqueous Medium. *J. Inorg. Organomet. Polym. Mater.* **2024**, *34*, 4742–4762. [CrossRef]
80. Rahman, M.; Rahman, M.L.; Biswas, B.; Ahmed, M.F.; Ali Shaikh, M.A.; Jahan, S.A.; Sharmin, N. Fabrication of novel ternary g-C_3N_4/Zn0.5Ni0.5Fe1.8Mn0.2O4/rGO hybrid nanocomposites for humidity sensing. *Nanoscale Adv.* **2025**, *7*, 1489–1504. [CrossRef]
81. Dubey, P.; Kaurav, N.; Devan, R.S.; Okram, G.S.; Kuo, Y.K. The effect of stoichiometry on the structural, thermal and electronic properties of thermally decomposed nickel oxide. *RSC Adv.* **2018**, *8*, 5882–5890. [CrossRef]

82. Xu, S.S.; Wang, Q.Q.; Lai, C.W.; Li, J.X. Rapid Preparation of C_3N_4/MgO Composites by Thermal Exfoliation Method and Their Photocatalytic Degradation Properties. *Russ. J. Phys. Chem. B* **2025**, *19*, 878–886. [CrossRef]
83. Dong, J.; Zhang, Y.; Hussain, M.I.; Zhou, W.; Chen, Y.; Wang, L.-N. g-C3N4: Properties, Pore Modifications, and Photocatalytic Applications. *Nanomaterials* **2022**, *12*, 121. [CrossRef]
84. Dahiya, S.; Sharma, A.; Chaudhary, S. Eco-inspired synthesis of MgO-infused g-C_3N_4 nanocomposites from tulsi seeds for advanced photocatalytic environmental remediation. *Phys. Chem. Chem. Phys.* **2024**, *26*, 28064–28081. [CrossRef]
85. Alaghmandfard, A.; Ghandi, K. A Comprehensive Review of Graphitic Carbon Nitride (g-C_3N_4)–Metal Oxide-Based Nanocomposites: Potential for Photocatalysis and Sensing. *Nanomaterials* **2022**, *12*, 294. [CrossRef]
86. Ndiaye, D.; Akill, A. A critical review on g-C_3N_4 for environmental remediation: Synthesis, properties, and pollutant photodegradation. *Rend. Lincei Sci. Fis. E Nat.* **2025**, *36*, 1139–1163. [CrossRef]
87. Wang, D.; Astruc, D. The recent development of efficient Earth-abundant transition-metal nanocatalysts. *Chem. Soc. Rev.* **2017**, *46*, 816–854. [CrossRef] [PubMed]
88. Yuan, C.; Wu, H.B.; Xie, Y.; Lou, X.W. Mixed Transition-Metal Oxides: Design, Synthesis, and Energy-Related Applications. *Angew. Chem. Int. Ed.* **2014**, *53*, 1488–1504. [CrossRef] [PubMed]
89. Ma, J.; Li, D. Interfacial regulation of photoanodes for photoelectrochemical water splitting: The roles of the interlayer and overlayer. *J. Mater. Chem. A* **2025**, *13*, 20200–20233. [CrossRef]
90. Goodman, D.W. Chemical modification of chemisorptive and catalytic properties of nickel. *Appl. Surf. Sci.* **1984**, *19*, 1–13. [CrossRef]
91. Jin, Z.; Jia, Y.; Zhang, K.-S.; Kong, L.-T.; Sun, B.; Shen, W.; Meng, F.-L.; Liu, J.-H. Effective removal of fluoride by porous MgO nanoplates and its adsorption mechanism. *J. Alloys Compd.* **2016**, *675*, 292–300. [CrossRef]
92. Hu, J.; Song, Z.; Chen, L.; Yang, H.; Li, J.; Richards, R. Adsorption Properties of MgO(111) Nanoplates for the Dye Pollutants from Wastewater. *J. Chem. Eng. Data* **2010**, *55*, 3742–3748. [CrossRef]
93. Mangaiyarkkarasi, J.; Sasikumar, S.; Meenakumari, V.; Revathy, J.S. A multidimensional approach to understanding wide band gap MgO: Structural, morphological, optical, and electron density insights. *MRS Adv.* **2024**, *9*, 870–875. [CrossRef]
94. Manikandan, S.; Sasikumar, D.; Seenivasan, S. Structural modification of g-C3N4 with NiO nanoparticles for superior photocatalytic removal of organic pollutants. *Ionics* **2025**. [CrossRef]
95. Eskalen, H.; Yaşar, D.; Kavgacı, M.; Yaykaşlı, H. Enhanced Photocatalytic Degradation of Methylene Blue Using g-$C_3N_4$4/NiCuFe2O4 Nanocomposites Under Visible Light Irradiation: A Study of Structural and Optical Characteristics. *J. Inorg. Organomet. Polym. Mater.* **2025**. [CrossRef]
96. Pantoja-Espinoza, J.C.; DelaCruz-Alderete, G.A.; Paraguay-Delgado, F. Photocatalytic Degradation of Methylene Blue Dye with g-C_3N_4/ZnO Nanocomposite Materials Using Visible Light. *Catalysts* **2025**, *15*, 851. [CrossRef]
97. Zhou, D.; Li, D.; Chen, Z. Recent advances in ternary Z-scheme photocatalysis on graphitic carbon nitride based photocatalysts. *Front. Chem.* **2024**, *12*, 1359895. [CrossRef]
98. Banu, A.; Sikdar, S.; Sinha, B. Design a promising nickel oxide embedded graphitic carbon nitride photocatalyst using for fast degradation of Indigo carmine dye. *Res. Chem. Intermed.* **2026**, *52*, 105–127. [CrossRef]
99. Fernández-Catalá, J.; Greco, R.; Navlani-García, M.; Cao, W.; Berenguer-Murcia, Á.; Cazorla-Amorós, D. g-C_3N_4-Based Direct Z-Scheme Photocatalysts for Environmental Applications. *Catalysts* **2022**, *12*, 1137. [CrossRef]
100. Salehi, G.; Bagherzadeh, M.; Abazari, R.; Hajilo, M.; Taherinia, D. Visible Light-Driven Photocatalytic Degradation of Methylene Blue Dye Using a Highly Efficient Mg–Al LDH@g-C_3N_4@Ag3PO4 Nanocomposite. *ACS Omega* **2024**, *9*, 4581–4593. [CrossRef]
101. Zhang, Y.; Lian, P.; Hao, X.; Zhang, L.; Yang, L.; Jiang, L.; Zhang, K.; Liao, L.; Qin, A. Modification Strategies of g-C_3N_4-Based Materials for Enhanced Photoelectrocatalytic Degradation of Pollutants: A Review. *Inorganics* **2025**, *13*, 225. [CrossRef]
102. Saafie, N.; Sufian, S.; Mufti, N.; Samsudin, M.F.R. The role of g-C3N4 loadings in MXene for photocatalytic degradation of methylene blue. *J. Mater. Sci. Mater. Electron.* **2025**, *36*, 389. [CrossRef]
103. Kumari, S.; sharma, S.; Kumari, M.; Singh, M.K.; Prasad, R.K.; Lee, K.-g.; Singh, D.K. Carbon Nitride: Physical properties and Applications. *arXiv* **2025**, arXiv:2506.20140. [CrossRef]
104. Xu, X.; Pan, Y.; Ge, L.; Chen, Y.; Mao, X.; Guan, D.; Li, M.; Zhong, Y.; Hu, Z.; Peterson, V.K.; et al. High-Performance Perovskite Composite Electrocatalysts Enabled by Controllable Interface Engineering. *Small* **2021**, *17*, 2101573. [CrossRef] [PubMed]